

Origin of the visible emission of black silicon microstructures

Filippo Fabbri,^{1,2,a)} Yu-Ting Lin,³ Giovanni Bertoni,¹ Francesca Rossi,¹ Matthew J. Smith,² Silviya Gradečak,² Eric Mazur,^{3,4} and Giancarlo Salvati^{1,a)}

¹IMEM-CNR Institute, Parco Area delle Scienze 37/A, 43124 Parma, Italy

²Department of Materials Science and Engineering, Massachusetts Institute of Technology, 77 Massachusetts Avenue, Cambridge, Massachusetts 02139, USA

³School of Engineering and Applied Sciences, Harvard University, 29 Oxford Street, Cambridge, Massachusetts 02138, USA

⁴Department of Physics, Harvard University, 17 Oxford Street, Cambridge, Massachusetts 02138, USA

(Received 12 May 2015; accepted 6 July 2015; published online 15 July 2015)

Silicon, the mainstay semiconductor in microelectronics, is considered unsuitable for optoelectronic applications due to its indirect electronic band gap that limits its efficiency as light emitter. Here, we univocally determine at the nanoscale the origin of visible emission in microstructured black silicon by cathodoluminescence spectroscopy and imaging. We demonstrate the formation of amorphous silicon oxide microstructures with a white emission. The white emission is composed by four features peaking at 1.98 eV, 2.24 eV, 2.77 eV, and 3.05 eV. The origin of such emissions is related to SiO_x intrinsic point defects and to the sulfur doping due to the laser processing. Similar results go in the direction of developing optoelectronic devices suitable for silicon-based circuitry. © 2015 AIP Publishing LLC. [<http://dx.doi.org/10.1063/1.4926912>]

Developing efficient silicon light emitters is crucial for integrating optoelectronic devices into silicon-based circuits. However, bulk cubic silicon has an indirect band gap of 1.1 eV and poor infrared light emission efficiency. Recent reports demonstrate room-temperature visible light emission in silicon in low-dimensional system, such as wurtzite silicon nanowires,^{1,2} nanocrystals,^{3,4} nano-pillars,⁵ porous silicon,^{6–8} and silicon/insulator superlattices.^{9,10} In addition, a simple femtosecond-laser (fs-laser) processing technique can drastically change the optical properties of silicon. In particular, the fs-laser processed silicon (black silicon) has gained increased interest due to the peculiar optical properties, including the enhanced sub-bandgap absorption^{11–13} and visible light emission.^{14,15}

In this work, we carry out cathodoluminescence spectroscopy and imaging in the scanning electron microscope (SEM-CL) and in the scanning transmission electron microscope (STEM-CL) to determine the black silicon light emission properties from the microscale to the nanoscale. We demonstrate that an intense visible emission comes from amorphous SiO_x microstructures, as inferred from structural and compositional analyses carried out using transmission electron microscopy (TEM) based techniques. Cathodoluminescence spectroscopy and imaging have two main advantages: the high energy electron probe excites even insulator materials as silicon oxide,¹⁶ and the high spatial resolution allows mapping at the nanoscale.¹⁷ The possibility of a controlled formation of SiO_x microstructures can open a scenario in the development of optoelectronic devices suitable for silicon-based circuitry.

We irradiated n-type silicon (100) wafers by 88 Ti:sapphire fs-laser pulses (800-nm wavelength, 80-fs pulse duration, and 700-μm spot size) at a fluence of 4 kJ/m². This process dopes silicon with sulfur due to the presence of SF₆

(500 Torr) in the atmosphere.^{11,12,18} Cross-sectional TEM samples were prepared using a tripod polisher followed by a brief Ar⁺-ion mill at 5 kV.

SEM-CL spectroscopy and imaging were carried out in a S360 Cambridge SEM equipped with a commercial Gatan MONOCLII system. The spectra are collected at an accelerating voltage of 10 keV with an injection power density equal to 2×10^6 W/cm². STEM-CL investigations were performed in a JEOL JEM-2011 equipped with a commercial Gatan MONOCL3 system¹⁹ using the accelerating voltage of 80 keV and a spot size of 5 nm. We perform all the CL experiments at room temperature. However, we note that the comparison between SEM-CL and STEM-CL spectra is non-trivial. The SEM-CL analysis was carried out at 10 keV in plan-view, with a corresponding generation-recombination volume of about 3.6×10^9 nm³, evaluated by means of a Monte Carlo simulation.²⁰ In the case of STEM-CL, the generation-recombination volume is about 1.2×10^4 nm³, estimated from a TEM lamella thickness of about 150 nm and an accelerating voltage of 80 keV. The difference in the generation-recombination volume leads to a largely different release of the electron beam energy in the specimen. Therefore, different spectral sensitivity and component intensity from SEM-CL and STEM-CL depend on different set-up and injection power conditions used in the SEM and STEM modes, respectively. The CL spectra were deconvoluted using a standard Levenberg-Marquardt algorithm to minimize the chi-square. As a result of the fitting, all peak positions are affected by an error of 0.01 eV, which is less than the error from the spectral resolution of the measurement (0.05 eV or 5 nm). *A* and *w* have an approximate error of 5%.

Energy filtered TEM (EFTEM) maps, energy disperse X-ray (EDX) spectroscopy, and electron energy loss spectroscopy (EELS) analyses were carried out in a Schottky emission gun JEOL JEM-2200FS equipped with an Omega filter. Relative thickness maps were derived as $t/\lambda = \ln(I_t/I_0)$,

^{a)}Authors to whom correspondence should be addressed. Electronic addresses: filippo.fabbri@imem.cnr.it and giancarlo.salvati@cnr.it

where I_t is an unfiltered image (approximately containing all scattered intensity) and I_0 is an elastic (or zero-loss) filtered image obtained using a 10 eV slit, and therefore is given in units of electron mean free path in the material (λ).

Figures 1(a) and 1(b) show the large area survey of the black silicon microstructure (BSMS) by SEM and panchromatic CL imaging, respectively. The inset of Figure 1(a) presents the morphology of the sample imaged at a 30° viewing angle. The large area CL panchromatic survey (Figure 1(b)) reveals the presence of BSMS with a high CL contrast. We define the CL contrast as

$$C(\%) = \frac{I_{Loc} - I_{Aver}}{I_{Aver}}, \quad (1)$$

where the I_{Loc} is the local CL intensity, and the I_{Aver} is the average CL intensity of the background. The bright CL contrast is evaluated to be between the 188% and 213%, for the area reported in Figure 1(b). A statistical study on a 0.5 cm²-sample reveals that 4% of the BSMS have a CL contrast between 150% and 250%.

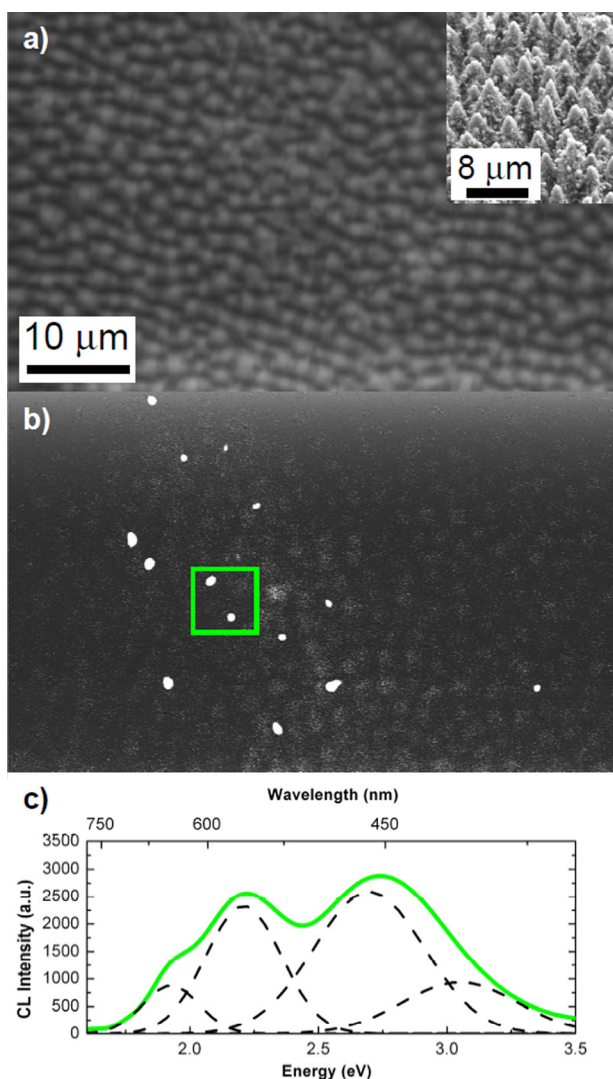


FIG. 1. (a) SE survey of black silicon; inset: 30° tilted SE image of the same sample. (b) Panchromatic SEM-CL map. (c) SEM-CL spectrum, taken from the area highlighted by the green square.

To further evaluate the origin of the bright emission, we obtained SEM-CL spectrum in the area highlighted by the green square in Figure 1(b). The CL spectrum shows a broad band in the visible range that can be deconvoluted into 4 Gaussian peaks centered at 3.05 eV, 2.77 eV, 2.24 eV, and 1.98 eV. The sum of the four components gives rise to the resultant white light emission. To investigate the structural origin of the visible emission, we identified one of the bright CL contrast regions of the sample and investigated it using TEM and CL-STEM. STEM-CL spectrum, reported in Figure 2(a), shows a similar lineshape to the SEM-CL spectrum of Figure 1(c), therefore it is used as benchmark for the recognition of bright CL contrast BSMS. Figures 2(b) and 2(c) show the bright field STEM image and the STEM-CL panchromatic map of the region with bright CL contrast. The panchromatic CL map reveals bright CL contrast areas in the BSMS.

Figures 3(a) and 3(b) show the zero loss image and the thickness map of the same area analyzed in STEM-CL. The zero-loss image shows the interruption of the strain induced lines, due to BSMS amorphization during femtosecond pulsed laser irradiation. The comparison between the zero-loss image (Figure 3(a)) and the CL-STEM panchromatic map (Figure 2(c)) reveals that the area with a bright CL-contrast does not show any strain induced lines and the crystalline areas do not present any light emission. This effect demonstrates that the visible light-emission is strictly related to the amorphization of the BSMS. The CL-STEM intensity is strongly dependent on the sample thickness; the inhomogeneous thinning of the sample is probably related to the interface between amorphous silicon oxide and crystalline silicon. In addition, [110] zone axis diffraction patterns (Figures 3(c) and 3(d)) were taken in the area without the strain-induced lines (blue circle) and on the crystalline silicon (red circle), respectively. The diffraction pattern from the substrate (Figure 3(d)) shows good crystallinity with characteristic (111), (200), and (022) Si reflections;

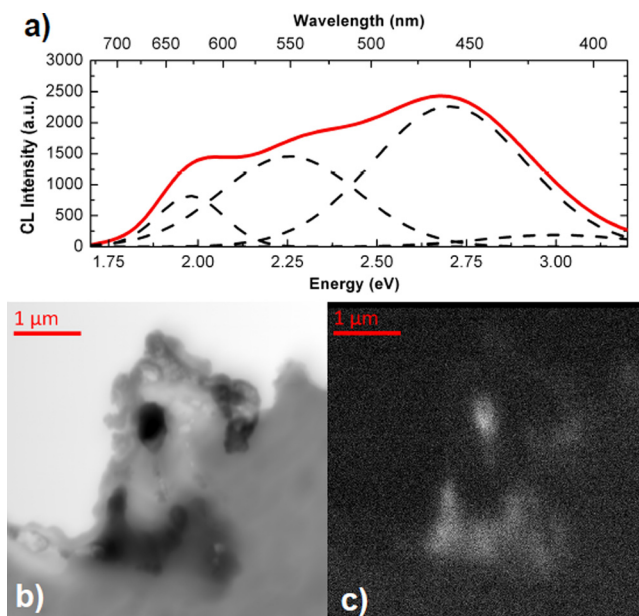


FIG. 2. (a) STEM-CL spectrum. (b) bright-field STEM of the BSMS/silicon interface area. (c) Panchromatic STEM-CL map.

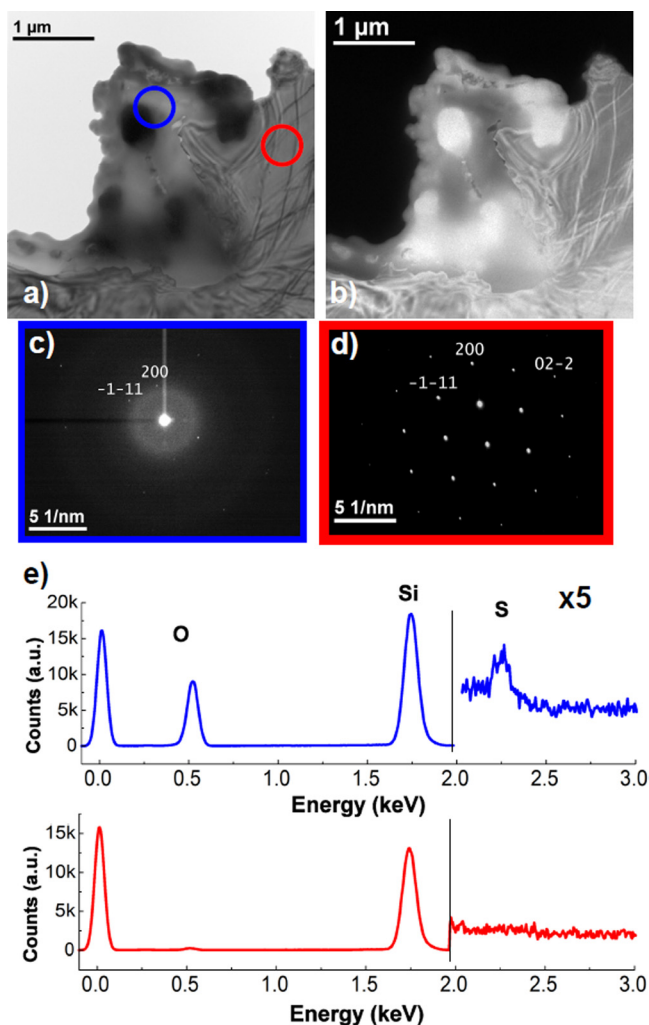


FIG. 3. (a) Zero-loss filtered image of the BSMS/silicon interface area. (b) Thickness map obtained from filtered and unfiltered images (in the map bright regions are thicker). (c) and (d) Selective area diffraction patterns from the BSMS (blue circle) and from the substrate (red circle). (e) EDX spectra taken in the BSMS (blue circle) and from the substrate (red circle). The EDX counts between 2 keV and 3 keV are multiplied by 5, in order to highlight the sulfur peak.

meanwhile, the BSMS diffraction pattern (Figure 3(c)) shows only weak spots from the (111) and (200) planes on a diffused background, confirming the amorphization of the BSMS. TEM-EDX spectra (Figure 3(e)) of the BSMS and of substrate were taken in spot mode in the same areas highlighted in Figure 3(a), revealing the stoichiometry and the presence of sulfur in the BSMS. In fact, the EDX quantitative analysis reveals that the BSMS is composed by SiO_x ,

with $x = 1.7$ and the sulfur concentration, close to the resolution limit of the EDX system, is about 1%.

The EFTEM maps of silicon, oxygen, and sulfur are reported in Figures 4(a), 4(b), and 4(c), respectively. Silicon and oxygen maps have an inverted contrast, indicating a high concentration of oxygen in the amorphous area, which demonstrates the occurrence of an oxidation of the BSMS. The sulfur EFTEM map from the S-L_{2,3} edge indicates a segregation at the interface between amorphous and crystalline silicon. However, the large average thickness of the sample lowers the precision in quantification or mapping,²¹ making the detection of the low amount of sulfur impractical. Moreover, the thicker regions in the sample look dark in the elemental maps due to wrong background extrapolation, a common limitation of EFTEM in the case of thick specimens.

We have demonstrated that the BSMS with the bright CL contrast are composed of SiO_x ; therefore, we can assign the different components to the visible emissions of this material.²² The 2.77-eV and 1.98-eV bands are attributed to intrinsic radiative recombination of amorphous silicon oxide: the silicon oxygen deficiency center (SiODC-II) and the surface non-bridging oxygen hole center (NBOHC).²² The attributions of such bands are supported by the stoichiometry evaluation, carried out by TEM-EDX analysis. The origin of the 2.24-eV band is still under debate. Recent works suggest that a 2.3-eV emission is related to carbon-doping of under stoichiometric silicon oxide¹⁶ or to silicon clustering related E_δ center.²³ However, the most probable attribution of this band is the understoichiometric silicon oxide self-trapped exciton,²⁴ considering that no carbon is found in EDX analysis and no silicon clustering effect is reported in the EFTEM mapping. Considering the previous work on black silicon luminescence,¹⁴ the 2.3-eV (540-nm) and the 1.98-eV (630-nm) emissions are attributed to silicon oxide defects and to the confined exciton in silicon nanoclusters, respectively. As for the 1.98-eV emission, the EFTEM analysis carried here does not reveal any silicon clustering effect. Finally, the peak at 3.05 eV is ascribed to the presence of sulfur dopant in the silicon oxide matrix, as demonstrated by previous works reporting CL spectroscopy of sulfur ion implanted SiO_2 films.^{25,26} The presence of sulfur in the SiO_x microstructure is confirmed by the EDX spectroscopy (Figure 3(e)) and EELS mapping (Figure 4(c)).

The formation of the amorphous silicon oxide BSMS can be ascribed to the possible structural instabilities induced by femtosecond pulsed laser processing^{18,27–29} and to the high concentration of sulfur atoms, used for the silicon doping over the limit of solubility.¹² Recent work demonstrates

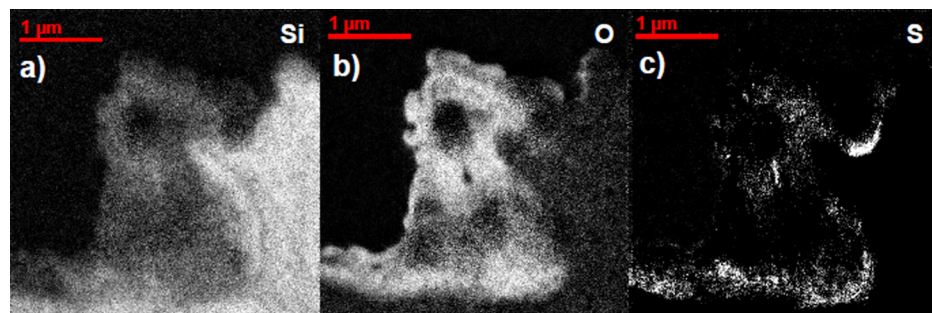


FIG. 4. (a)–(c) EFTEM maps of silicon, oxygen, and sulfur.

that the structural instabilities can depend on the number of laser pulses, pressure of the dopant precursor, and the presence of silicon native oxide.³⁰ Similarly as reported for boron doping, the formation of amorphous silicon areas is promoted by doping at high concentration.³¹ In addition, doping segregation at the interface between amorphous silicon oxide and crystalline silicon was reported for arsenic doping,³² in agreement with sulfur segregation reported in Figure 4(c).

In conclusion, we determined the origin of the visible light emission of black silicon microstructures. The bright CL contrast microstructures are found to consist of amorphous silicon oxide microstructures, as demonstrated by the structural and compositional measurements. CL-SEM panchromatic mapping reveals the presence of 4% microstructures with a bright CL contrast (between 188% and 213%). The broad visible emission is composed by four features, peaked at 1.98 eV, 2.24 eV, 2.77 eV, and 3.05 eV, related to intrinsic or extrinsic radiative centers of silicon oxide. Inducing a visible emission is promising for the development of silicon-based white-light emitting devices. These would permit easy integration with silicon-based circuits.

The authors would like to acknowledge Dr. S. Chen of the MIT Center of Material Science and Engineering (CMSE) for supporting the STEM-CL measurements. Part of this work was supported by the U.S. Air Force Office of Scientific Research Contract No. FA9550-14-1-0150.

¹F. Fabbri, E. Rotunno, L. Lazzarini, D. Cavalcoli, A. Castaldini, N. Fukata, K. Sato, G. Salviati, and A. Cavallini, *Nano Lett.* **13**, 5900 (2013).

²F. Fabbri, E. Rotunno, L. Lazzarini, N. Fukata, and G. Salviati, *Sci. Rep.* **4**, 3603 (2014).

³W. L. Wilson, P. F. Szajowski, and L. E. Brus, *Science* **262**, 1242 (1993).

⁴L. Pavesi, L. Dal Negro, C. Mazzoleni, G. Franzo, and F. Priolo, *Nature* **408**, 440 (2000).

⁵A. G. Nassiopoulou, S. Grigoropoulos, and D. Papadimitriou, *Appl. Phys. Lett.* **69**, 2267 (1996).

⁶L. T. Canham, *Appl. Phys. Lett.* **57**, 1046 (1990).

⁷A. G. Cullis and L. T. Canham, *Nature* **353**, 335 (1991).

⁸K. D. Hirschman, L. Tsybeskov, S. P. Duttagupta, and P. M. Fauchet, *Nature* **384**, 338 (1996).

⁹S. Cuffe, C. Labbe, B. Dierre, F. Fabbri, T. Sekiguchi, X. Portier, and R. Rizk, *J. Appl. Phys.* **108**, 113504 (2010).

¹⁰Z. H. Lu, D. J. Lockwood, and J. M. Baribeau, *Nature* **378**, 258 (1995).

¹¹M. T. Winkler, M.-J. Sher, Y.-T. Lin, M. J. Smith, H. Zhang, S. Gradečak, and E. Mazur, *J. Appl. Phys.* **111**, 093511 (2012).

¹²M.-J. Sher, Y.-T. Lin, M. T. Winkler, E. Mazur, C. Pruner, and A. Asenbaum, *J. Appl. Phys.* **113**, 063520 (2013).

¹³M. Algasinger, J. Paye, F. Werner, J. Schmidt, M. S. Brandt, M. Stutzmann, and S. Koynov, *Adv. Energy Mater.* **3**, 1068 (2013).

¹⁴C. Wu, C. H. Crouch, L. Zhao, and E. Mazur, *Appl. Phys. Lett.* **81**, 1999 (2002).

¹⁵M. Ranjan Gartia, Y. Chen, and G. Logan Liu, *Appl. Phys. Lett.* **99**, 151902 (2011).

¹⁶F. Fabbri, F. Rossi, M. Negri, R. Tatti, L. Aversa, S. C. Dhanabalan, R. Verucchi, G. Attolini, and G. Salviati, *Nanotechnology* **25**, 185704 (2014).

¹⁷F. Fabbri, M. Villani, A. Catellani, A. Calzolari, G. Cicero, D. Calestani, G. Calestani, A. Zappettini, B. Dierre, T. Sekiguchi, and G. Salviati, *Sci. Rep.* **4**, 5158 (2014).

¹⁸M. J. Smith, M.-J. Sher, B. Franta, Y.-T. Lin, E. Mazur, and S. Gradečak, *J. Appl. Phys.* **112**, 093511 (2012).

¹⁹S. K. Lim, M. Brewster, F. Qian, Y. Li, C. M. Lieber, and S. Gradečak, *Nano Lett.* **9**, 3940 (2009).

²⁰D. Drouin, A. R. Couture, D. Joly, X. Tastet, V. Aimez, and R. Gauvin, *Scanning* **29**, 92 (2007).

²¹G. Bertoni and J. Verbeeck, *Ultramicroscopy* **108**, 782 (2008).

²²L. Skuja, *J. Non-Cryst. Solids* **239**, 16 (1998).

²³H. Nishikawa, E. Watanabe, D. Ito, Y. Sakurai, K. Nagasawa, and Y. Ohki, *J. Appl. Phys.* **80**, 3513 (1996).

²⁴A. N. Trukhin, M. Goldberg, J. Jansons, H. J. Fitting, and I. A. Tale, *J. Non-Cryst. Solids* **223**, 114 (1998).

²⁵H.-J. Fitting, *J. Lumin.* **129**, 1488 (2009).

²⁶R. Salh, B. Schmidt, and H. J. Fitting, *Phys. Status Solidi A* **202**, R53 (2005).

²⁷J. Jia, M. Li, and C. V. Thompson, *Appl. Phys. Lett.* **84**, 3205 (2004).

²⁸J. Bonse, S. Baudach, J. Krüger, W. Kautek, and M. Lenzner, *Appl. Phys. Lett.* **74**, 19 (2002).

²⁹M. S. Amer, M. A. El-Ashry, L. R. Dosser, K. E. Hix, J. F. Maguire, and B. Irwin, *Appl. Surf. Sci.* **242**, 162 (2005).

³⁰M.-J. Sher, N. M. Mangan, M. J. Smith, Y.-T. Lin, S. Marbach, T. M. Schneider, S. Gradečak, M. P. Brenner, and E. Mazur, *J. Appl. Phys.* **117**, 125301 (2015).

³¹X. Q. Yan, X. M. Huang, S. Uda, and M. W. Chen, *Appl. Phys. Lett.* **87**, 191911 (2005).

³²C. Y. Wong, C. R. M. Grovenor, P. E. Batson, and R. D. Isaac, *J. Appl. Phys.* **58**, 1259 (1985).